Effect of Tacticity on the Molecular Dynamics of Polypropylene Melts

Stelios J. Antoniadis, Christina T. Samara, and Doros N. Theodorou*

Molecular Modelling of Materials Laboratory, Institute of Physical Chemistry, National Research Centre for Physical Sciences "Demokritos", GR 15310 Ag. Paraskevi Attikis, Greece, and Department of Chemical Engineering, University of Patras, GR 26500 Patras, Greece

Received June 3, 1999; Revised Manuscript Received August 1, 1999

ABSTRACT: In this work we present the results of molecular dynamics simulations of polypropylene melts of different tacticities, based on a recently published molecular model. Volumetric properties of isotactic, syndiotactic, and atactic polypropylene exhibit no significant differences and are in good agreement with experimental data. The simulated X-ray diffraction patterns agree well with experimental scattering results, suggesting that the simulated structure is realistic. Methyl−methyl intramolecular distribution functions exhibit several peaks characteristic of the conformations adopted by each tacticity. Conformational distributions of dyads reveal a preference for *tg* conformers in isotactic polypropylene (iPP) and for *tt* in syndiotactic polypropylene (sPP), which is closely related to the type of helices observed in the crystalline form. Time autocorrelation functions have been computed for pendant ($C-CH_3$) bonds and skeletal torsion angles. Predicted correlation times are found to be shortest for the iPP melt and longest for the sPP melt; a simple estimation of barriers to $t \rightarrow g$ conformational transitions explains this difference in the dynamics.

1. Introduction

Tailoring molecular structure to achieve desired performance characteristics is of paramount importance in all technological applications involving polymers. As performance specifications become more demanding and as the variety and complexity of monomers, polymers, and copolymers available increases, it is becoming increasingly time-consuming and expensive to optimize polymer systems through experimental trial-and-error synthesis or phenomenological correlations alone. To ensure competitiveness, it is crucial that research and development scientists have reliable predictive tools to guide experiments for developing new polymeric systems and improving existing ones. These tools must provide insights at the molecular level into how details of the molecular structure and specific chemical interactions affect the final material properties.

Particularly important from the viewpoint of applications are vinyl polymers, because they offer the opportunity to tailor properties through appropriate selection of the tacticity of chains. In this work we focus on a representative vinyl polymer, polypropylene (PP), whose rapidly expanding range of applications has led to a 7% annual increase of industrial production in the United States.[1] Polypropylene is synthesized in three different tacticities, atactic (aPP), isotactic (iPP), and syndiotactic (sPP). The microstructure of PP is a critical determinant of the polymer physical properties. aPP is totally amorphous with a glass transition temperature (T_g) of approximately 255 K, and iPP and sPP are semicrystalline at room temperatures. The melting points of iPP and sPP are strongly affected by the crystallizability of the chains, which depends in turn on defects in their stereochemical structure (percentage of meso [*m*] and racemo [*r*] dyads up to pentads [*mmmm*] or [*rrrr*] along the backbone).[2] The melting points calculated from extrapolation of experimental results are 433−460 K for perfect iPP[2−5] (100% meso dyads) and 433−455 K for perfect sPP[6,7] (100% racemo dyads).

There has been considerable modeling work on PP.[8−13] Several simulation techniques have been employed, such as molecular mechanics,[8] molecular dynamics (MD),[9−11] and Monte Carlo[12] (MC) for the purpose of predicting elastic constants in the glassy state, melt and glass volumetric (PVT) properties, surface tension, gas solubility, and some aspects of dynamical behavior. Despite the encouraging results obtained, the PP models used in these past investigations have not been completely satisfactory. In a previous work[14] we presented a molecular model suitable for predicting thermodynamic and dynamical properties of PP. We tested this model on aPP melts using MD simulations and found very good agreement of volumetric behavior and segmental dynamics with experimental data for a wide range of temperatures and pressures.

In this paper we continue our study with emphasis on tactic PP melts and we try to investigate and explain how tacticity affects dynamical properties. Section 2 briefly presents the molecular model and the simulation details. Results on PVT behavior, structure, and segmental dynamics for various tacticities are presented and discussed in Section 3, followed by a statement of conclusions drawn from this work (Section 4). Finally, details of the theoretical analysis are presented in the Appendix.

2. Molecular Model and Simulation Method

The model system consisted of $N_{ch} = 2$ molecules of degree of polymerization $N_{un} = 76$ in a cubic cell of initial side 25 Å with periodic boundary conditions. In our model, the chains are composed of carbon (C), hydrogen (H), and methyl (R) Lennard−Jones (LJ) interaction sites. C−C and C−R bond lengths are fixed at 1.54 Å, whereas CCC and CCR skeletal bond angles are flexible. All mass is assumed to be concentrated on R and C sites, i.e., the mass of each hydrogen is collapsed onto the carbon atom to which it is connected. In this way high-frequency vibrating HCH bond angles are excluded, permitting a significantly longer time step in the

* Author to whom correspondence should be addressed at the University of Patras (Phone: +3061-997-398; Fax: +3061-993-255; E-mail: doros@sequoia.chemeng.upatras.gr).

10.1021/ma990888f CCC: $18.00
Published on Web 11/11/1999

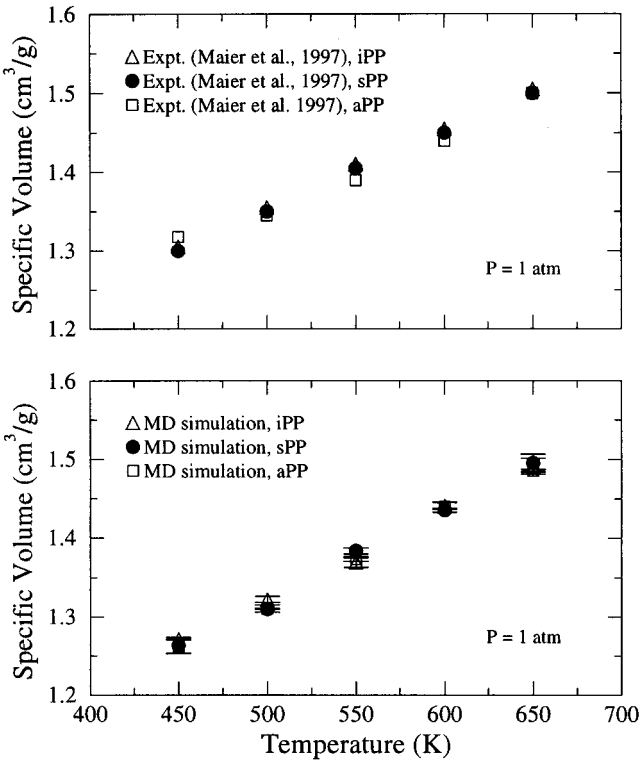

Figure 1. Dependence of the specific volume of iPP, aPP, and sPP at $P = 1$ atm on temperature as predicted by simulation, and as measured experimentally.[15]

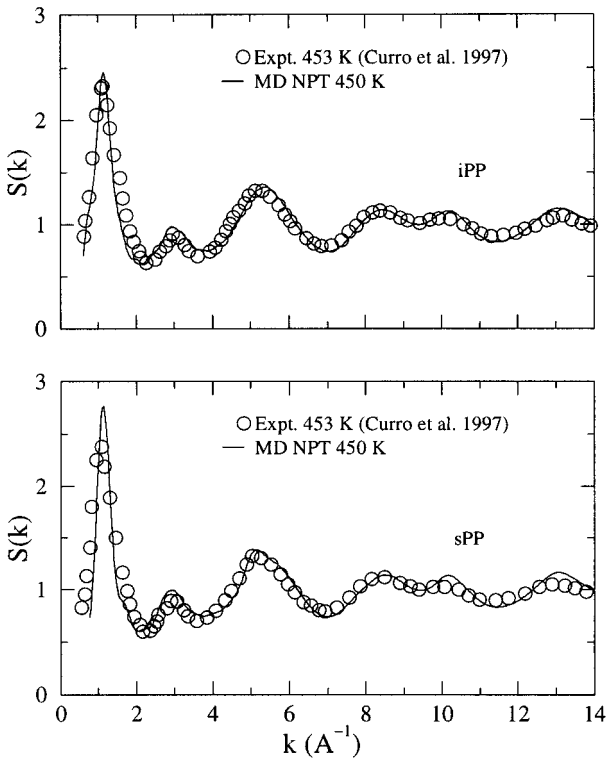

Figure 2. Simulated and experimental X-ray diffraction patterns of iPP and sPP at 450 K. The experimental measurements are from Curro et al.[17]

MD simulation. Positions of pendant hydrogens are uniquely determined by the surrounding heavy (C and R) interaction sites, with C−H bonds kept constant at l_H =1.10 Å. A detailed description of the positioning of hydrogens, the potential parameters used, and the MD simulation algorithm is given in ref 14. Simulations were performed at a pressure P of 1 atm and temperatures T ranging from 450 to 650 K. Six initial configurations were produced through molecular mechanics,[8] two for each tacticity, and equilibrated for 100−1000 ps, depending on the temperature simulated. The fraction of meso dyads was 48%, 100%, and 0% for aPP, iPP, and sPP, respectively. To achieve better equilibration, we first performed runs at the highest temperature and then used the last configuration as input for the next run at lower temperature. Stabilization of the running average for the density and the various components of the energy was used as a criterion for starting data collection, i.e., starting the "production phase" of the run. Most properties were obtained from analysis of 1-ns-long production trajectories, but two 5-ns-long runs were also undertaken to explore long-time dynamics and confirm convergence of the simulation estimates.

3. Results and Discussion

PVT Behavior. With the potential parameterization adopted,[14] satisfactory predictions are achieved for the volumetric properties over a wide range of temperatures and pressures for all tacticities. The predicted specific volume at $P = 1$ atm is shown as a function of temperature in Figure 1. Error bars result from averaging the data of isothermal−isobaric (NPT) MD runs started at the two different initial configurations. The experimental values[5,15] almost coincide for the three PP melts, as do the simulated values in the whole temperature range. Moreover, simulated values are lower than, but always within 3% of experiment, as also reported in the previous paper[14] for aPP melts.

Structural Features. The structure of the polymer melts was examined by calculating the simulated X-ray diffraction pattern. The static structure factor at a given wave vector **k** is defined as

$$S(k) = 1 + \frac{\left\langle \frac{1}{V} \right\rangle \sum_a \sum_b N_a N_b f^a(k) f^b(k) \int [g^{ab}(r) - 1] e^{-i\mathbf{k}\cdot\mathbf{r}} d^3r}{\sum_a [N_a f^a(k)]^2} \quad (1)$$

The radial distribution functions $g^{ab}(r)$ for each pair of groups (a, b) in the system (a, b = CH, CH_2, CH_3) and the inverse system volume $1/V$ were accumulated and averaged for each structure, at a given temperature. The terms N_a and $f^a(k)$ are the number and atomic scattering factor, respectively, of atomic groups of type a. The atomic scattering factors of CH, CH_2, and R = CH_3 were calculated through an analytical approximation described in ref 16. In Figure 2 simulated diffraction patterns are presented along with experimental data[17] for iPP and sPP at 450 K; analogous results for aPP were presented previously.[14] Here we obtained the experimental $S(k)$ from equation 10a of ref 17, which we normalized with the factor

$$N_{un} / \sum_a [N_a f^a(k)]^2$$

in order that it be equivalent with our calculated $S(k)$. The positions and magnitudes of the major intermolecular peak near $k = 1.1$ Å^{-1} and of the intramolecular peaks near 3.0 and 5.0 Å^{-1} agree well with experiment, indicating that the structures of the simulated polymers are realistic and almost identical. The simulation predicts a somewhat sharper intermolecular peak for sPP, which is related to the larger conformational

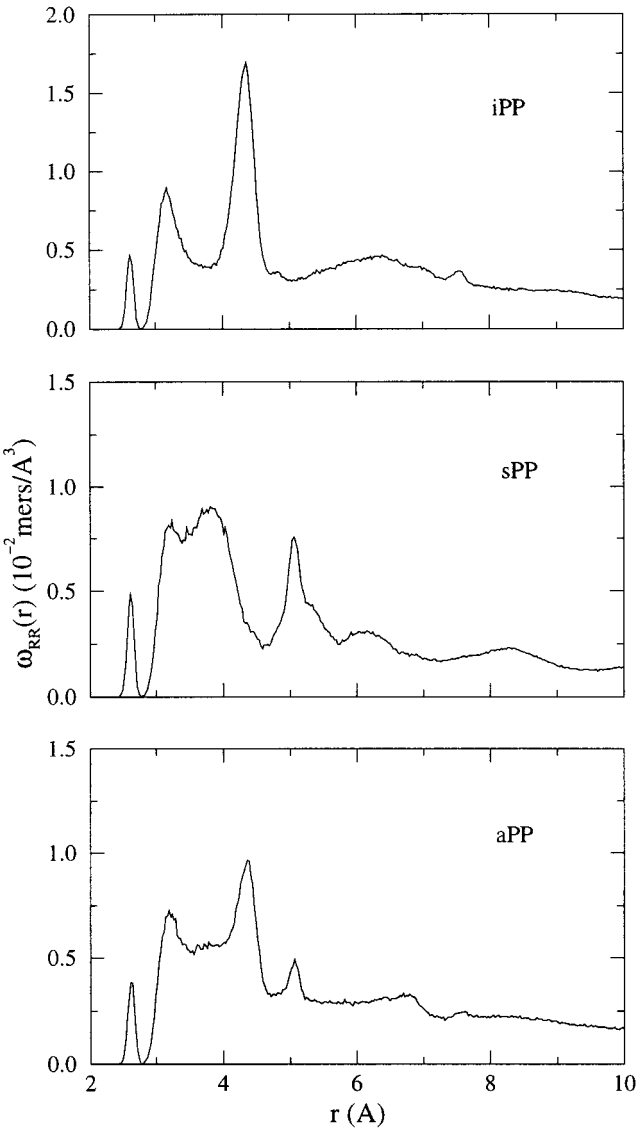

Figure 3. Intramolecular pair density functions of methyl groups $\omega_{RR}(r)$ for iPP, aPP, and sPP at 450 K.

stiffness exhibited by this tacticity. Such a difference in the structure is not observed in the experimental scattering patterns, however.

To discuss the basic characteristics of intramolecular structure of PP melts, we present in Figure 3 the intramolecular pair density function[18] $\omega(r)$ of methyl groups at 450 K for the three tacticities. As expected, there is a significant difference between the two tactic forms (isotactic and syndiotactic), resulting from differences in chain conformation. The conformations of PP according to Suter and Flory[19] present five rotational isomeric states ($\bar{g}$, *t*, *t**, *g**, *g*) with $\bar{g}$, *t*, *g* being the dominant states, as seen from aPP studies.[14] To understand the conformations adopted by iPP and sPP in the melt, it is useful to consider the conformations adopted by these polymers in the crystalline state.

The crystalline structure of iPP involves only one helical conformation, a 3_1−helix with 6.5 Å chain axis repeat distance.[20] The helix (*tgtgtg*...) is based on *tg* dyad conformations, which avoid RR steric conflicts. The major peak seen in the methyl−methyl $\omega(r)$ of the isotactic melt at 4.3 Å is characteristic of *tg* conformations as well, whereas the broad peak around 6.3 Å is a vestige of the pitch of helix-like $(tg)_3$ and $(tg)_2$ conformations. In addition, the peak at 3.2 Å is characteristic of $t\bar{g}$ conformations and the small peak at 7.6 Å originates in $tgt\bar{g}tg$ conformations. The pattern obtained here exhibits the same peaks as the intramolecular structure function $\Omega_{RR}(r)$, extracted from single-chain MC simulations of united and explicit atom models, that is presented in ref 17.

Although sPP can exist in an all-trans conformation,[6] its stable crystalline structure[21] is based on a sequence of $(ttgg)_2$ conformations resulting in a 4_2−helix of repeat distance of 7.4 Å. The peaks at 3.2 and 3.8 Å in the $\omega(r)$ function of the syndiotactic melt are characteristic of the *tt* conformation; the sharp peak at 5.2 Å and the broad peak at 8.2 Å are characteristic of *tttt* and *tttttt* conformations, respectively. The broad peak at 6.1 Å illustrates the *ttgg*, *tggt* conformations. This pattern identifies the strong tendency of sPP to adopt long sequences of *t* conformations, and also exhibit some of the characteristics of a $(ttgg)_2$ helix.

The aPP ω_{RR} exhibits almost all the peaks of the two tactic forms, but with reduced intensity. The peak at 2.6 Å that is present in all three diagrams of Figure 3 is due to the pairs of methyls that appear at chain ends.

In Figure 4 three chains from the simulated melts, one of each tacticity, are plotted at 650 K. Clearly, sPP has many sequences of *t* conformations that force it into the most extended form; on the contrary, iPP with many *tg* conformations adopts less extended conformations, and aPP exhibits intermediate behavior. A detailed study of characteristic ratios for iPP, sPP, and aPP in the melt is currently carried out using the end-bridging MC algorithm. Results will be reported in a future publication.

The three intermolecular radial distribution functions for CC, CR, and RR pairs are shown in Figure 5. The reader should note that these results are based on a model box of linear dimension ca. 25 Å, in which approximately 40% of the intermolecular neighbors of each group belong to periodic images of the chain containing the group. Simulations with different box sizes would be required to establish unequivocally the system-size independence of predicted intermolecular structural features. By comparison of these plots, it can be seen that the packing of iPP, aPP, and sPP in the melt is rather similar. A smaller correlation hole effect[22] and somewhat sharper structure is predicted for sPP; its more extended chains can come closer together and develop somewhat more organized structures. Comparing our results to analogous plots of Curro et al.,[17] we find that our g_{C-C} plots are similar to their g_{CH-CH} plots, with their $g_{CH_2-CH_2}$ plots exhibiting a peak at 4 Å which does not appear in our g_{C-C} plots. Moreover, our g_{R-R} distribution functions are also in agreement with theirs, except for the first peak that is sharper, because of their use of the PRISM model. For the same reason, their g_{CH_2-R} and g_{CH-R} functions exhibit sharp peaks, whereas our g_{C-R} functions are rather smooth.

Torsional angle distributions at 650 K are presented in Figure 6. The five rotational isomeric states (RIS) for PP according to the conformational analysis of Suter and Flory[19] are also indicated in this figure. At this temperature, only $\bar{g}$, *t*, and *g* states are clearly detectable. The *t** state is completely merged with *t*, resulting merely in a skewness in the *t* peak. The *g** state appears as a raised baseline between *t* and *g* peaks. The $\bar{g}$ state is significantly more populated than is predicted by the RIS model.[8,14] The *t* state is significantly more populated

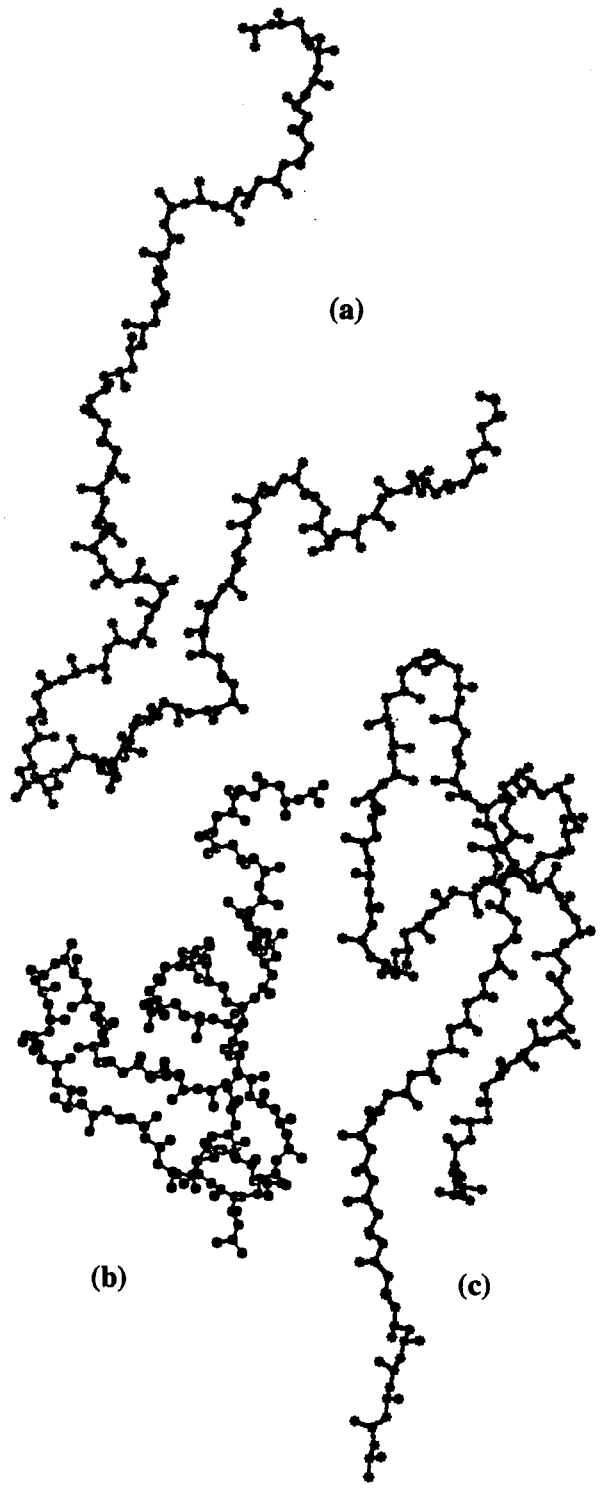

Figure 4. Snapshots of an (a) atactic, (b) isotactic, and (c) syndiotactic chain from melt simulations at 650 K.

in sPP than in iPP, whereas the *g* peak is higher in iPP than in sPP. The $\bar{g}$ peak for sPP is almost the same height as the *g* peak. Although successive torsion angles in sPP can readily form sequences of the energetically most favorable *t* states, in iPP such sequences necessarily have to be interrupted by *g* states, because they would lead to strong steric repulsions between the bulky methyl substituents. In the crystalline state, as already mentioned, this leads to different conformational sequences for the two tacticities, which, however, contain equal populations of *t* and *g* states. In the melt, it leads to a predominance of the *t* state in sPP.

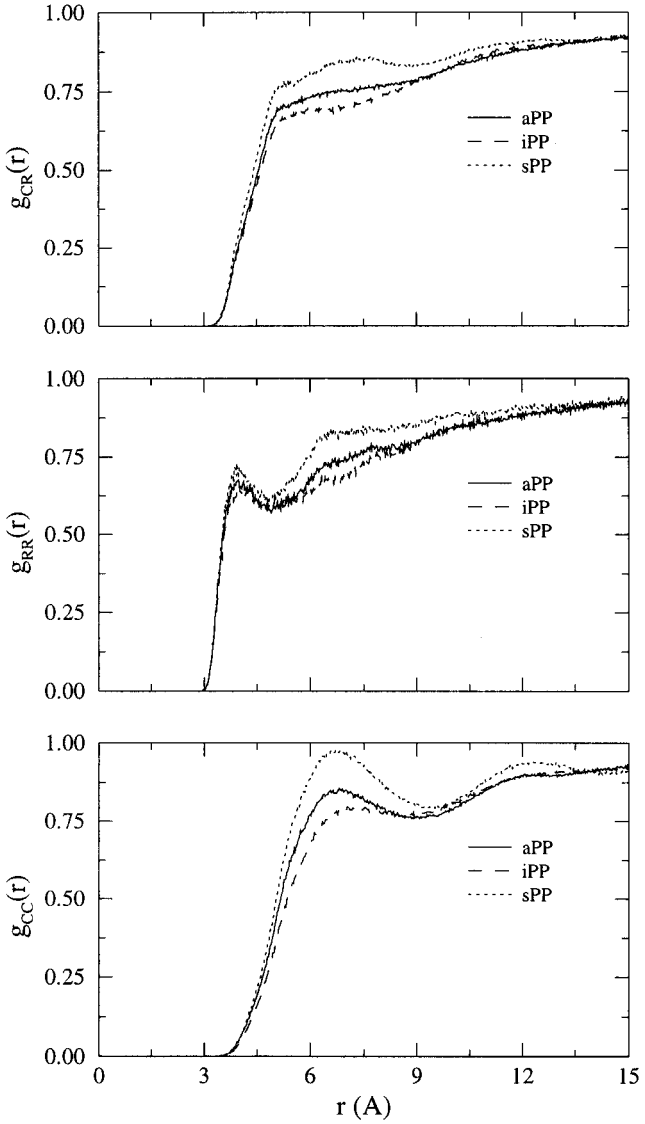

Figure 5. Intermolecular radial distribution functions of CR, RR, and CC pairs for all three tacticities examined.

For a better understanding of conformations we study the distributions of states adopted by pairs of successive torsion angles at 650 K. These distributions are shown at the top of Figure 7, along with separate distributions of states for $CH_2-CHR-CH_2$ and $CHR-CH_2-CHR$ pairs of successive angles. It is clear that the percentage of *tg* conformers is high in iPP, exceeding 50%; this is consistent with the 66% calculated by Suter and Flory[19] at 400 K. The next important pair conformation in iPP is *tt*, which has almost half the height of *tg*. On the contrary, in sPP *tt* pairs are clearly most preferred, which supports the dominance of trans sequences in the melt. The *tg* and $t\bar{g}$ in sPP are less than half as probable as *tt*, and practically equally populated. As displayed in the middle and bottom diagrams, *tg* states in sPP are adopted mainly by $CH_2-CHR-CH_2$ pairs of torsion angles, because for $CHR-CH_2-CHR$ pairs of angles these states result in a close approach of a methyl to the chain backbone. On the contrary, although not highly populated, *gg* states are adopted mainly by $CHR-CH_2-CHR$ pairs of angles, because for $CH_2-CHR-CH_2$ these states result in a "hairpin" conformation that brings two parts of the backbone too close. The conformational distribution of pairs of successive torsion

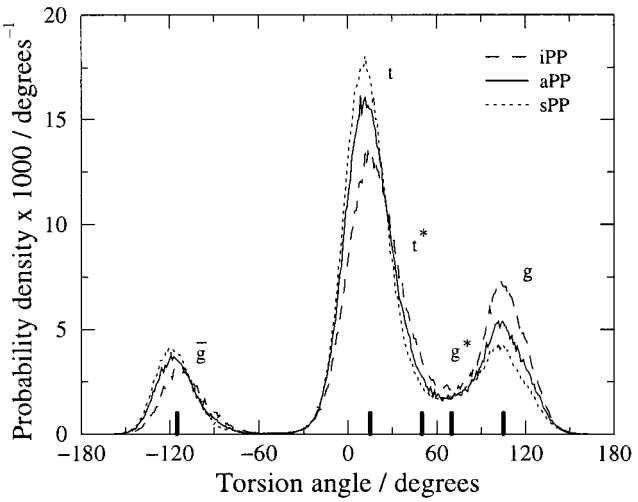

Figure 6. Simulated torsion angle distributions of iPP, sPP, and aPP melts. Results are shown for atmospheric pressure and $T = 650$ K. The convention for measuring torsion angles is as in ref 8. Trans (t, t^*) and gauche ($\bar{g}$, g^*, g) rotational isomeric states are denoted. The discrete locations of the five states in the rotational isomeric state of Suter and Flory[19] are marked.

angles for aPP is in-between those of iPP and sPP for all significantly populated pairs of states.

Segmental Dynamics. Local dynamics was investigated by monitoring the rate of reorientation of C−R vectors. As in ref 14, the directional autocorrelation functions for C−R vectors are defined as

$$P_1(i, t) = \langle \mathbf{u}_{CR}(i, t) \cdot \mathbf{u}_{CR}(i, 0) \rangle \quad (2)$$

$$P_2(i, t) = \frac{1}{2}(3\langle [\mathbf{u}_{CR}(i, t) \cdot \mathbf{u}_{CR}(i, 0)]^2 \rangle - 1) \quad (3)$$

where $\mathbf{u}_{CR}(i, t)$ is the unit vector along C_i-R_i bond at time t. The autocorrelation functions were fit with the Kohlrausch−Williams−Watts (KWW) equation

$$P_{KWW}(t) = \exp[-(t/\tau)^{\beta}] \quad (4)$$

where τ is a characteristic time and β is the stretching exponent. Following the procedure discussed in ref 14 we can estimate the correlation times for C−R bond orientational relaxation as

$$\tau_c = \int_0^{\infty} P_2(t)\, dt \rightarrow \tau_c = \tau \frac{\Gamma\left(\frac{1}{\beta}\right)}{\beta}$$

β values from the fit are found to be 0.40−0.46 for iPP, 0.36−0.39 for aPP, and 0.30−0.37 for sPP, the higher values corresponding to higher temperatures for each tacticity. The resulting τ_c can be directly compared with NMR experiments. One-nanosecond-long runs were sufficient for unequivocal determination of τ_c at these high temperatures. The temperature dependence of τ_c is non-Arrhenius. In Figure 8 the τ_c values obtained from the simulation are plotted for each tacticity along with Williams−Landel−Ferry (WLF) curves fit to NMR experiments. Because no direct experimental measurements are available at these high temperatures, we present the two WLF curves proposed for aPP[23] and iPP[24] based on NMR data accumulated at lower temperatures. Fitting the WLF equation

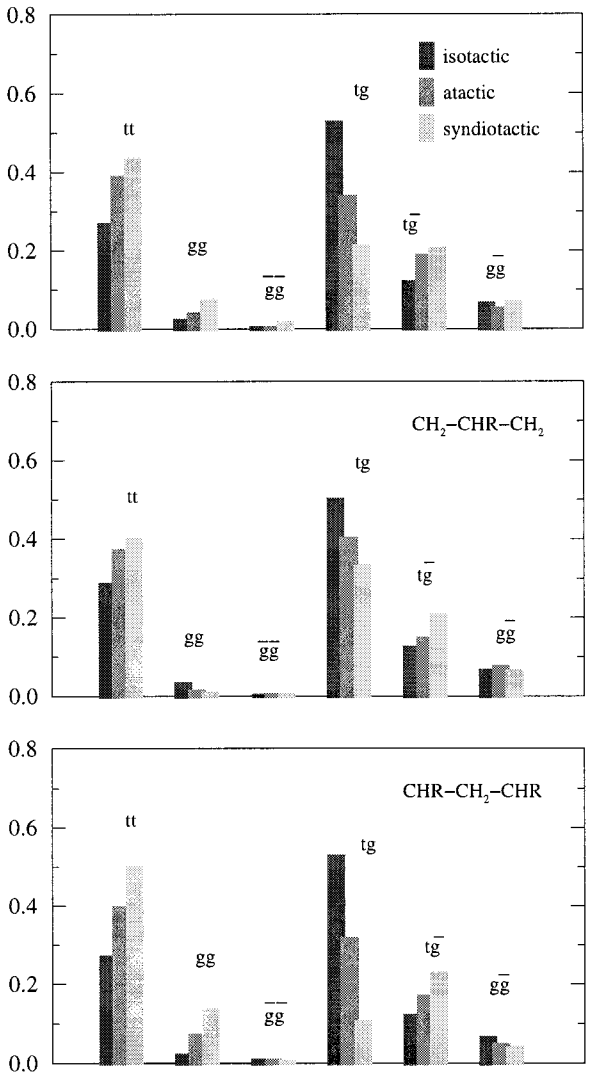

Figure 7. Distribution of pairs of successive torsion angles among rotational states for the three tacticities.

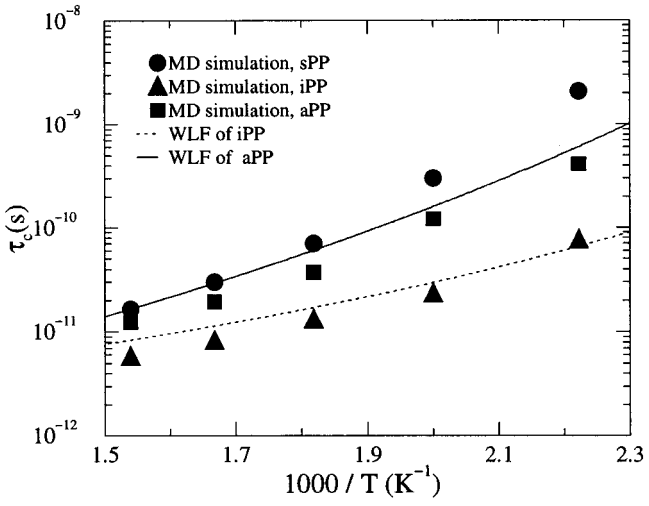

Figure 8. Temperature dependence of characteristic relaxation times for iPP, aPP, sPP bond vector orientational decorrelation, averaged over many runs initiated at two different configurations. Simulated values are calculated from KWW fits to the $P_2(t)$ function via $\tau_c = \tau\Gamma(1/\beta)/\beta$.

$$\log \frac{\tau(T)}{\tau(T_g)} = -\frac{C_1(T - T_g)}{C_2 + T - T_g} \quad (5)$$

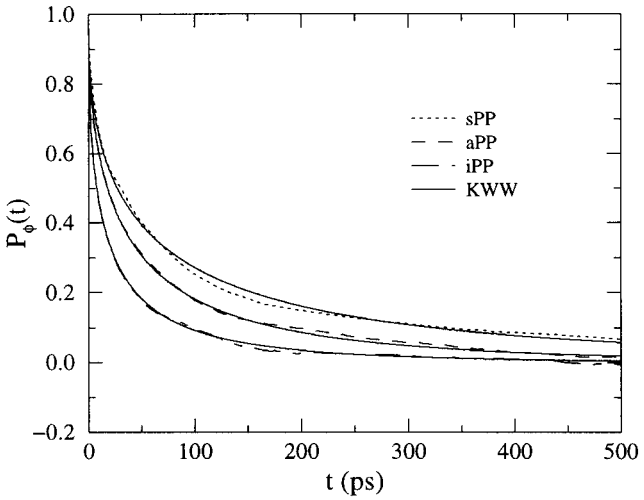

Figure 9. Simulated torsional autocorrelation function $P_\phi(t)$ for various tacticities, along with KWW fits at 650 K.

to NMR data from iPP, Zemke et al.[24] obtained the following values for the constants: $C_1 = 14.5$, $C_2 = 30$ K. The analogous parameters obtained by Dekmezian et al.[23] for aPP were $C_1 = 15.2$, $C_2 = 60.7$ K. In plotting eq 5, we have used[24] $\tau(T_g) = 100$ s and $T_g = 255$ K for both tacticities. The difference in τ_c between iPP and aPP is in very favorable agreement with the extrapolated experimental WLF curves. According to our simulation, iPP exhibits clearly the lowest relaxation times, sPP the highest, and aPP lies in the middle at all temperatures. The important result here is that the three tacticities do not have the same relaxation times in the melt as they have near T_g.[24] It is also evident that the difference in relaxation times between iPP and sPP becomes larger as the temperature approaches T_m. This behavior could be explained by the more efficient intermolecular packing of sPP chains (Figure 5).

To further clarify the segmental dynamics, we monitor the torsional angle autocorrelation function

$$P_\phi(t) = \frac{\langle \cos \phi(t) \cos \phi(0) \rangle - \langle \cos \phi(0) \rangle^2}{\langle \cos \phi(0) \cos \phi(0) \rangle - \langle \cos \phi(0) \rangle^2} \qquad (6)$$

where $\phi(t)$ is the torsion angle at time t. P_ϕ functions for all three tacticities are displayed in Figure 9 at 650 K. At high temperature the decay is almost perfectly KWW,[14,25] indicating an abundance of correlated conformational transitions involving neighboring torsion angles, the multiplicity in local environments encountered by these angles giving rise to stretched exponential behavior. As expected, the curve for iPP goes faster to zero than the curves for sPP and aPP, which means that the relaxation time of $\phi(t)$ is smaller in iPP. This result is in agreement with our analysis of C−R bond orientational relaxation and supports that the iPP melt has faster dynamics than sPP, with aPP found somewhere in the middle.

Chain relaxation in polymers far above T_g is accomplished mainly through conformational isomerizations. Thus, in view of our relaxation results we expect that the rate of transitions between torsional states will depend on tacticity. To detect this dependence directly, we analyzed the conformational transitions using the definition of Weber and Helfand,[26] which considers a

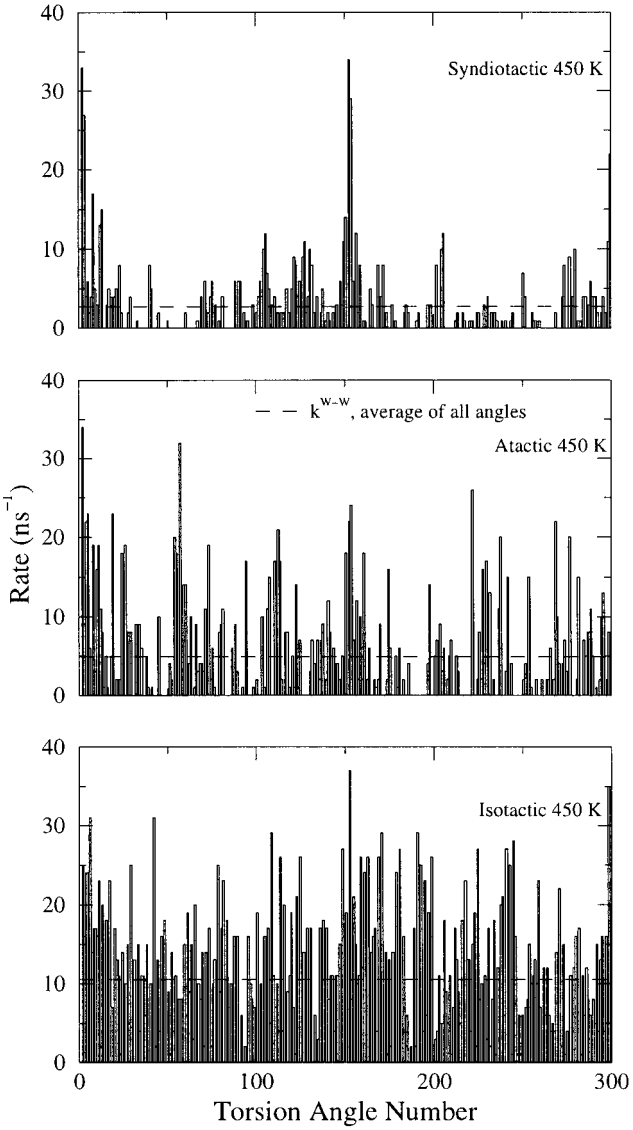

Figure 10. Individual conformational transition (well-to-well passage) rates for all torsion angles, calculated from 1-ns-long MD simulations at 450 K. The numbering convention used is such that angles 1−150 correspond to the first chain and 151−300 to the second chain. Dashed horizontal lines: average well-to-well passage rate at each tacticity.

transition of a torsion angle i to be complete only when ϕ_i has surmounted the potential barrier separating two conformational states and reached the bottom of the potential well of the new state. For the purposes of this analysis we considered a three-state rotational isomeric model, retaining only the $\bar{g}$, t, and g rotational states. The boundary between g and t states was placed at 60°. The overall rate, k^{W-W}, of well-to-well passages was calculated by[10]

$$k^{W-W} = N^{W-W}/N_\phi t_{run} \qquad (7)$$

where N^{W-W} is the total number of successful crossings between adjacent states, $N_\phi = 300$ is the total number of torsion angles in the system, and t_{run} is 1 ns. In Figure 10 conformational transition rates are shown for each ϕ_i, along with the average k^{W-W} at 450 K for the three tacticities. It is clear that transitions are less frequent on the average and less homogeneously distributed in sPP and aPP, where same-chain cooperativity is a critical factor, whereas in iPP torsional transitions occur

Table 1. Conformational Transition (Well-to-Well Passage) Rate Constants

	temperature (K)				
k^{W-W} (ns^{-1})	650	600	550	500	450
iPP	37.93	30.29	22.88	16.41	10.51
aPP	24.50	19.12	15.54	9.99	4.90
sPP	17.43	12.60	8.50	5.50	2.75

Table 2. Uncorrected Transition (Barrier Crossing) Rates for *t*→*g* Isomerization

rate	temperature (K)				
(ns^{-1} Å^{-3})	650	600	550	500	450
iPP	1.089	1.018	0.906	0.778	0.678
aPP	0.847	0.765	0.695	0.567	0.427
sPP	0.722	0.639	0.550	0.468	0.341

Table 3. Transition (Well-to-Well Passage) Rates for *t*→*g* Isomerization

rate	temperature (K)				
(ns^{-1} Å^{-3})	650	600	550	500	450
iPP	0.321	0.279	0.225	0.169	0.115
aPP	0.214	0.174	0.153	0.104	0.054
sPP	0.150	0.115	0.081	0.058	0.030

uniformly along the entire chain length. In Table 1 we present the overall rate constants at five temperatures for the three tacticities. In all cases, iPP exhibits the highest and sPP the lowest rate constant. Thus, the reason for the faster relaxation we have observed in iPP seems to be that much more transitions are taking place per unit time in iPP than in aPP and sPP. The ratio of conformational transition rates of iPP and sPP according to Table 1 is about 2 at 650 K and becomes approximately 4 for the lowest temperature studied (450 K).

Why is the conformational transition rate so much higher in iPP, even though densities are very comparable for the three tacticities? A closer look reveals that 91% of the observed transitions at 650 K and 98% of the observed transitions at 450 K occur between *t* and *g* states; these percentages are almost independent of the tacticity studied. This proves that the $t \rightleftharpoons g$ "reaction" is the dominant pathway for relaxation, the population of $\bar{g}$ states being almost isolated from *t* and *g* by high energy barriers (see Figure 6), so our further analysis focused on this "reaction". The rate of $t \rightarrow g$ transitions (transitions per unit time per unit volume of polymer) was found to be equal to the rate of $g \rightarrow t$ transitions to an excellent approximation (relative error: 0.1%), which means that the populations of the *t* and *g* states are well equilibrated at all temperatures and tacticities examined. We computed the $t \rightarrow g$ transition rate in three different ways. First, we counted the angles that passed the barrier between *t* and *g* states for $t_{run} = 1$ ns at each temperature (Table 2). Second, we counted only well-to-well transitions using the definition of Weber and Helfand, stated above (Table 3). Dynamical recrossing events are fully present in the numbers of Table 2, but are removed to a great extent from the numbers of Table 3, which thus are considerably lower. To calculate the rate constants of the reaction $t \rightarrow g$ we divided the number of transitions per unit time per unit volume, as counted in Table 3, by the volume concentration of angles in the *t* state. The results are shown in Table 4; they are similar to the k^{W-W} values listed in Table 1, with the only difference that they refer specifically to the $t \rightarrow g$ transition. The activation energies estimated from Table 4 are 3.5 kcal/mol for iPP, 4.6 kcal/mol for aPP, and 5.3 kcal/mol for sPP. The low activation energy of iPP permits a great number of transitions to occur, hence faster relaxation occurs compared to the two other tacticities.

Table 4. Rate Constants (Well-to-Well Passage) for *t*→*g* Isomerization

$k_{t\rightarrow g}$	temperature (K)				
(ns^{-1})	650	600	550	500	450
iPP	28.81	23.95	18.54	13.17	8.71
aPP	17.75	14.01	11.36	7.27	3.59
sPP	12.07	7.35	5.81	3.91	1.76

Table 5. Fraction of Rates for *t*→*g* Isomerization

	temperature (K)				
$Rate_{iso}/Rate_{syndio}$	650	600	550	500	450
barrier crossing (Table 2)	1.51	1.59	1.65	1.66	1.99
well-to-well (Table 3)	2.14	2.43	2.78	2.91	3.83
estimated from ϕ distribution	1.51	1.56	1.69	1.70	1.91
hazard plot	1.4				

A third way to estimate rates is to use the energy profile extracted from the population distributions among different states (Figure 6). A full description of this analysis is given in the Appendix. The rates extracted through this approach are uncorrected for dynamical recrossing events, i.e., they are comparable to those of Table 2. Ratios of $t \rightarrow g$ transition rates in iPP to the corresponding rates in sPP obtained by each of the three methods discussed above are presented in Table 5. In all cases the fraction is greater than 1, and a decreasing function of temperature. The barrier-crossing analysis and the calculation based on ϕ distributions yield very similar results.

The estimation of transition rates from the ϕ distributions affords a simple explanation of why the dynamics of iPP is so much faster than that of sPP, with aPP situated in the middle. To a reasonable approximation (see Figure 6) the *t* and *g* states can be viewed as energy wells which are isolated from the $\bar{g}$ state but communicate with each other through an energy barrier comparable to k_BT. The absolute height of the barrier ($-k_BT\ln(\rho^*)$ in the terminology of the Appendix) is roughly the same in iPP and in sPP. The mean depth ($-k_BT\ln(\rho_t\rho_g)^{1/2}$) of the *t* and *g* energy wells is roughly the same in iPP as it is in sPP and the shapes of the energy wells are also roughly the same. The two well depths, however, are much more disparate in sPP than in iPP. Under these conditions, the more disparate the wells, the lower the expected rate of transitions between them (see Appendix), which explains the results of Table 5.

A fourth way to calculate the rate of conformational transitions, which is perhaps the most preferable but also the most demanding computationally, is to construct hazard plots.[26] The hazard rate $h(t)$ is defined such that $h(t)dt$ is the probability that a bond, which has not had a transition in a time *t* since its last transition, undergoes a transition (first passage) between *t* and $t + dt$. The cumulative hazard function is defined as

$$H(t) = \int_0^t h(t')dt' \qquad (8)$$

The hazard plot was constructed as described in ref 14. For a Poisson process, the hazard plot would be a straight line with slope equal to the rate of conformational isomerization. Such behavior has been seen in

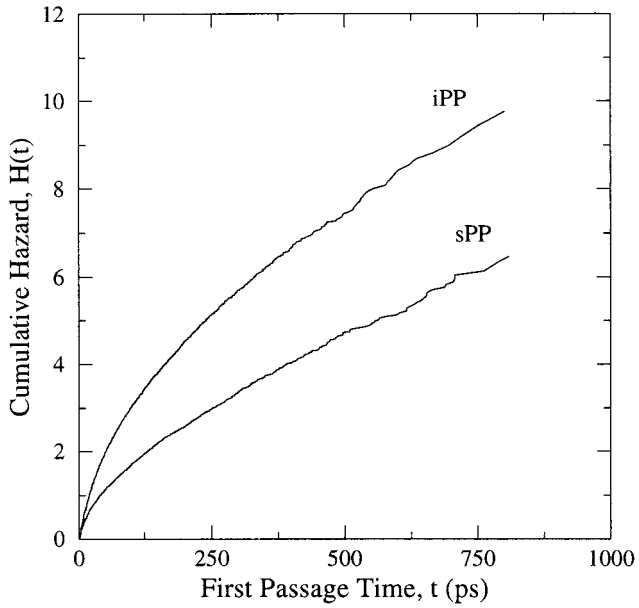

Figure 11. Hazard plot of first passage times for conformational transitions at 650 K for iPP and sPP.

MD simulations of polyethylene melts.[25] As shown in ref 14, such a rectilinear behavior is not seen in atactic PP out to times of 1 ns, even at the highest temperature studied (600 K). For this reason we perfomed here two longer runs (5 ns) for iPP and sPP at 650 K. As shown in Figure 11, linear behavior is indeed reached for the two tactic forms at times longer than 0.5 ns. From the slopes of the linear parts of the two curves we obtain estimates of the rate constants for conformational isomerization that should be completely free of the effects of recrossing events. These are 8.4 and 5.9 ns^{-1} for iPP and sPP, respectively. The values of these rate constants are smaller than the values based on counting well-to-well passages and listed in Table 1 by factors of 4.5 and 3.0, respectively. This is understandable, because rate constants based on well-to-well passages are not completely free of the effects of recrossing events occurring over the region separating *t* and *g* states. Clearly, the effect of recrossings is stronger for iPP than for sPP. This is also supported by the longer region of linearity observed for sPP in the hazard plot of Figure 11. The ratios of transition rate constants at 650 K based on the linear parts of the hazard plots, 1.4, is significantly lower than the corresponding ratio based on well-to-well passages, 2.1 (see Table 5). Interestingly, the ratio based on the hazard plot is quite close to the ratio 1.5 based on uncorrected barrier crossing rates or estimated from the distribution of torsion angles, shown in the same table.

4. Conclusions

In this work we presented results from MD simulations of PP melts of different tacticities, which were based on a recently published molecular model. Information on the structure and dynamics was accumulated from 1- and 5-ns-long NPT runs using two initial structures for each tacticity over a wide range of temperatures and at a pressure of $P = 1$ atm. The simulated specific volume vs temperature curves of iPP, sPP, and aPP exhibit no significant differences and are within 3% of experiment. The simulated X-ray diffraction patterns and intermolecular pair distribution functions suggest a somewhat sharper structure in the syndiotactic melt, which consists of stiffer chains; they are in reasonable agreement with available scattering measurements. Intramolecular pair density functions for methyls exhibit several peaks characteristic of the conformations adopted by each tacticity. Torsion angle distributions show that *t* states are more populated in sPP, *g* states are more populated in iPP. In addition, distributions of pairs of successive torsion angles revealed a preference for *tg* conformers in iPP and for *tt* in sPP. These conformational tendencies are reminiscent of the helices formed by the polymers in their crystalline form.

The segmental dynamics of the PP systems have been examined in several ways. Orientational autocorrelation functions have been calculated for pendant (C−R) bonds above the melting points of iPP and sPP. The temperature dependence of predicted correlation times, using KWW fits, exhibits a WLF behavior. Although close at high temperature, the correlation times diverge as the temperature approaches T_m, with iPP exhibiting faster motion at all temperatures. Simulated torsion angle autocorrelation functions display a KWW decay at the temperatures studied here and confirm the faster relaxation of iPP. Conformational transitions in the melt were analyzed by calculating the rates of the dominant $t \rightarrow g$ isomerizations through four different approaches. Transition rates for iPP are faster than for sPP by a factor of 1.5−2, which increases with decreasing temperature. The faster relaxation exhibited by iPP in comparison to sPP can be explained simply by envisioning the *t* and *g* states as two energy wells. The height of the barrier separating the states is roughly the same in iPP as in sPP, and also the mean depth of the *t* and *g* wells is roughly the same between the two tacticities. The difference in depth between *t* and *g* energy wells, however, is much greater in sPP than in iPP, leading to a significantly lower rate of transitions between the wells.

Interestingly, the difference in segmental dynamics between iPP and sPP as extracted from the rate of conformational isomerizations is much smaller than the difference in correlation times for pendant bond reorientation; values of τ_c in Figure 8 differ by a factor of 4−30 between iPP and sPP. The reason for this must be sought in the cooperativity of small-amplitude motions involved in C−R reorientation in the bulk.

Appendix

To understand the faster rates of $t \rightarrow g$ conformational isomerization, therefore the faster segmental dynamics exhibited by iPP as compared to sPP, we estimated the $t \rightarrow g$ transition rates through a transition-state theory (TST) approach based on the distributions of torsion angles shown in Figure 6. The rate of transitions $R_{1\rightarrow2}$ from state 1 to state 2, measured in transitions per unit volume per unit time, is expressed as

$$R_{1\rightarrow2} = k_{1\rightarrow2}C_1 \qquad \text{(A.1)}$$

where $k_{1\rightarrow2}$ is a rate constant (s^{-1}) and C_1 is the "concentration" of torsion angles in state 1. Since the total concentration of torsion angles, *C*, in the system remains constant and independent of tacticity, C_1 can be written as Cp_1, where p_1 is the fraction of torsion angles in state 1 (population of state 1).

The rate constant $k_{1\rightarrow2}$ can be expressed by invoking TST in the harmonic approximation[27] as

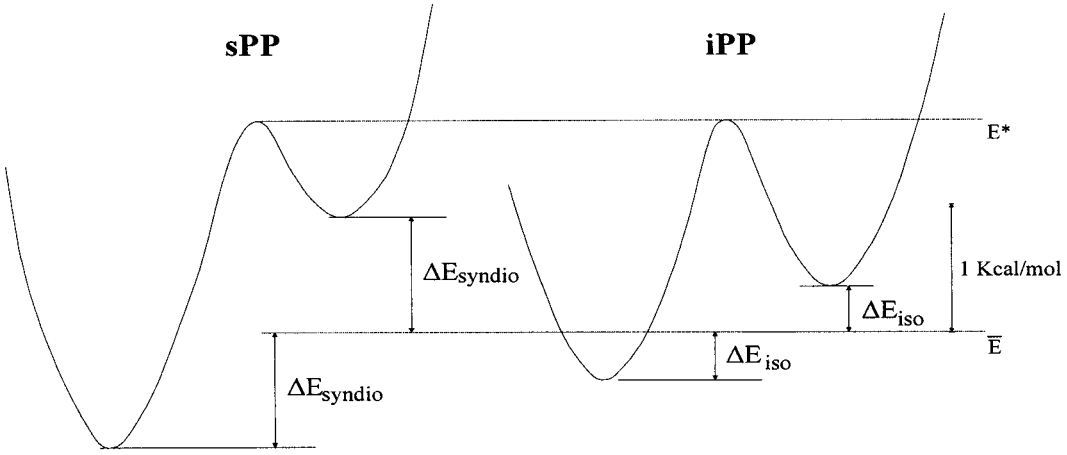

Figure 12. Simple depiction of the energetics of conformational transitions in isotactic and syndiotactic PP.

$$k_{1\rightarrow 2} = \nu_0 \, \mathrm{e}^{-(E^*-E_1)/k_\mathrm{B}T} \tag{A.2}$$

where E_1 is the energy of the local energy minimum (well bottom) corresponding to state 1, E^* is the energy of the transition state (top of barrier) between states 1 and 2, and ν_0 is a frequency of oscillation of the system within the well of state 1. ν_0 depends on the local curvature of the energy hypersurface around the minimum and around the saddle point, and is assumed to be independent of tacticity in this analysis. The difference $E^* - E_1$ represents the energy barrier that the system must overcome in effecting a transition from state 1 to state 2. Barrier recrossing events are neglected in the TST approximation. If entropic contributions associated with fluctuations around an energy well are assumed to be similar for all states, the equilibrium population of state 1 can be expressed as

$$p_1 = \frac{\mathrm{e}^{-E_1/k_\mathrm{B}T}}{\sum_i \mathrm{e}^{-E_i/k_\mathrm{B}T}} \tag{A.3}$$

where the index i runs over all states accessible to the system. Focusing on the transition $t \rightarrow g$ for an angle capable of assuming three torsional states (t, g, $\bar{g}$) and invoking A.1−A.3, we write the rate as

$$R_{t\rightarrow g} = \nu_0 C \mathrm{e}^{-(E^*-E_\mathrm{t})/k_\mathrm{B}T} \frac{\mathrm{e}^{-E_\mathrm{t}/k_\mathrm{B}T}}{\mathrm{e}^{-E_\mathrm{t}/k_\mathrm{B}T} + \mathrm{e}^{-E_\mathrm{g}/k_\mathrm{B}T} + \mathrm{e}^{-E_\bar{\mathrm{g}}/k_\mathrm{B}T}}$$

$$= \nu_0 C \frac{1}{\mathrm{e}^{(E^*-E_\mathrm{t})/k_\mathrm{B}T} + \mathrm{e}^{(E^*-E_\mathrm{g})/k_\mathrm{B}T} + \mathrm{e}^{(E^*-E_\bar{\mathrm{g}})/k_\mathrm{B}T}} \tag{A.4}$$

The quantities $E^* - E_t$, $E^* - E_g$, $E^* - E_{\bar{g}}$ can then be estimated from the values of the probability density, $\rho(\phi)$, plotted in Figure 6 at the saddle point between states t and g and at the maxima ϕ_t, ϕ_g, $\phi_{\bar{g}}$ corresponding to the three torsional states:

$$E^* - E_i = -k_\mathrm{B}T \ln\left(\frac{\rho^*}{\rho_i}\right) \qquad i = t, g, \bar{g} \tag{A.5}$$

Combining A.4 and A.5:

$$R_{t\rightarrow g} = \nu_0 C \frac{\rho^*}{\rho_t + \rho_g + \rho_{\bar{g}}}$$

Furthermore, comparing rates between the syndiotactic and isotactic form,

$$\frac{(R_{t\rightarrow g})_\mathrm{iso}}{(R_{t\rightarrow g})_\mathrm{syndio}} = \frac{\rho^*_\mathrm{iso}}{\rho^*_\mathrm{syndio}} \frac{(\rho_t + \rho_g + \rho_{\bar{g}})_\mathrm{syndio}}{(\rho_t + \rho_g + \rho_{\bar{g}})_\mathrm{iso}} \tag{A.6}$$

The values reported in the third row of Table 5 were obtained from the $\rho(\phi)$ distribution of Figure 6 and its counterparts at other temperatures using eq A.6.

To illustrate the reason for the difference in dynamics in the simplest possible terms, we introduce the additional approximation that the population of the $\bar{g}$ state is roughly the same for the two tacticities. This approximation can be justified by comparing the areas under the $\bar{g}$ peaks in Figure 6. Furthermore, we will assume that the $\bar{g}$ population does not change significantly with temperature, because the $\bar{g}$ state is more or less isolated from t and g by high energy barriers and very few transitions occur from or into it. Then,

$$p_{\bar{g},\mathrm{iso}} = \left(\frac{\mathrm{e}^{-E_\bar{\mathrm{g}}/k_\mathrm{B}T}}{\mathrm{e}^{-E_\mathrm{t}/k_\mathrm{B}T} + \mathrm{e}^{-E_\mathrm{g}/k_\mathrm{B}T} + \mathrm{e}^{-E_\bar{\mathrm{g}}/k_\mathrm{B}T}}\right)_\mathrm{iso}$$

$$= p_{\bar{g},\mathrm{syndio}} = \left(\frac{\mathrm{e}^{-E_\bar{\mathrm{g}}/k_\mathrm{B}T}}{\mathrm{e}^{-E_\mathrm{t}/k_\mathrm{B}T} + \mathrm{e}^{-E_\mathrm{g}/k_\mathrm{B}T} + \mathrm{e}^{-E_\bar{\mathrm{g}}/k_\mathrm{B}T}}\right)_\mathrm{syndio}$$

at all temperatures. Using the latter equality in eq A.4, one can readily prove:

$$\frac{(R_{t\rightarrow \mathrm{g}})_\mathrm{iso}}{(R_{t\rightarrow \mathrm{g}})_\mathrm{syndio}} = \frac{(\mathrm{e}^{(E^*-E_\mathrm{t})/k_\mathrm{B}T} + \mathrm{e}^{(E^*-E_\mathrm{g})/k_\mathrm{B}T})_\mathrm{syndio}}{(\mathrm{e}^{(E^*-E_\mathrm{t})/k_\mathrm{B}T} + \mathrm{e}^{(E^*-E_\mathrm{g})/k_\mathrm{B}T})_\mathrm{iso}} \tag{A.7}$$

From the distributions of Figure 6 we see that it is not unreasonable to assume $(E^* - E_t)_\mathrm{iso} + (E^* - E_g)_\mathrm{iso} \simeq (E^* - E_t)_\mathrm{syndio} + (E^* - E_g)_\mathrm{syndio} = 2E$. Setting $E^* - E_t = E + \Delta E$ for each tacticity,

$$\frac{(R_{t\rightarrow g})_\mathrm{iso}}{(R_{t\rightarrow g})_\mathrm{syndio}} = \frac{\mathrm{e}^{\Delta E_\mathrm{syndio}/k_\mathrm{B}T} + \mathrm{e}^{-\Delta E_\mathrm{syndio}/k_\mathrm{B}T}}{\mathrm{e}^{\Delta E_\mathrm{iso}/k_\mathrm{B}T} + \mathrm{e}^{-\Delta E_\mathrm{iso}/k_\mathrm{B}T}} = \frac{\cosh(\Delta E_\mathrm{syndio}/k_\mathrm{B}T)}{\cos\,\mathrm{h}(\Delta E_\mathrm{iso}/k_\mathrm{B}T)} > 1 \tag{A.8}$$

because $\Delta E_\mathrm{syndio} > \Delta E_\mathrm{iso} > 0$ and, for positive x, cosh x is an increasing function of its argument.

The situation described by the simple model, eq A.7, is represented pictorially in Figure 12. We have two pairs of states with a barrier in between. The average well depth of the two states relative to the barrier, $\bar{E} - E^*$, is the same for both pairs but the difference between the well depths, $2\Delta E$, is considerably larger in the syndiotactic pair than in the isotactic pair. As seen from eq A.8, the pair with the smaller disparity between the well depths will exhibit a higher transition rate. Thus, iPP exhibits faster dynamics than sPP basically because the two dominant conformational states, *t* and *g*, are energetically closer in iPP, even though the height of the barrier separating these states relative to their mean well depth is the same in both tacticities.

Note Added in Proof

We have recently become aware that Shaun M. Lippow, Xiao-Hua Qiu, and Prof. Mark D. Ediger of the University of Wisconsin are performing ^{13}C NOE and τ_1 NMR measurements on iPP and sPP melt in the temperature range examined in this work. These new measurements should allow a more direct comparison of our predictions against experiment than is shown in Figure 8.

References and Notes

(1) Moore, E. P. *Polypropylene Handbook*; Hansen Publishers: New York, 1996.
(2) Madkour, T. M.; Mark, J. E. *J. Polym. Sci. Polym. Phys.* **1997**, *35*, 2757.
(3) Petraccone, V.; Guerra, G.; De Rosa, C.; Tuzi, A. *Macromolecules* **1985**, *18*, 813.
(4) Cheng, S. Z.; Janimak, J. J.; Zhang, A.; Cheng, H. N. *Macromolecules* **1990**, *23*, 298.
(5) Sato, Y.; Yamasaki, Y.; Takishima, S.; Masuoka, H. *J. Appl. Polym. Sci.* **1997**, *66*, 141.
(6) Rodriguez-Arnold, J.; Zhang, A.; Cheng, S. Z. D.; Lovinger, A. J.; Hsieh, E. T.; Chu, P.; Johnson, T. W.; Honnell, K. G.; Geerts, R. G.; Palackal, S. J.; Hawley, G. R.; Welch, M. B. *Polymer* **1994**, *35*, 1884.
(7) De Rosa, C.; Auriemma, F.; Vinti, V.; Galimberti, M. *Macromolecules* **1998**, *31*, 6206.
(8) Theodorou, D. N.; Suter, U. W. *Macromolecules* **1985**, *18*, 1467.
(9) Sylvester, M. F.; Yip, S.; Argon, A. S. In *Computer Simulation of Polymers;* Roe, R.-J., Ed.; Prentice Hall: Englewood Cliffs, NJ, 1991; p 105.
(10) Mansfield, K. F.; Theodorou, D. N. *Macromolecules* **1991**, *24*, 6283.
(11) Han, J.; Boyd, R. H. *Macromolecules* **1994**, *27*, 5365.
(12) Boone, T. D. Prediction of Glass-Melt Behavior and Penetrant Sorption Thermodynamics in Vinyl Polymers via Molecular Simulations. Ph.D. Thesis, University of California at Berkeley, 1995.
(13) Greenfield, M. L.; Theodorou, D. N. *Macromolecules* **1998**, *31*, 7068.
(14) Antoniadis, S. J.; Samara, C. T.; Theodorou, D. N. *Macromolecules* **1998**, *31*, 7944.
(15) Maier, R. D.; Thomann, R.; Kressler, J.; Mülhaupt, R. *J. Polym. Sci. Polym. Phys.* **1997**, *35*, 1135.
(16) Narten, A. H. *J. Chem. Phys.* **1979**, *70*, 299.
(17) Curro, J. G.; Weinhold, J. D.; Rajasekaran, J. J.; Habenshuss, A.; Londono, J. D.; Honeycutt, J. D. *Macromolecules* **1997**, *30*, 6264.
(18) Dodd, L. R.; Theodorou, D. N. *Adv. Polym. Sci.* **1994**, *116*, 249.
(19) Suter, U. W.; Flory, P. J. *Macromolecules* **1975**, *8*, 765.
(20) Lotz, B.; Wittmann, J. C.; Lovinger, A. J. *Polymer* **1996**, *37*, 4979.
(21) Corradini, P.; Natta, G.; Ganis, P.; Tempussi, P. A. *J. Polym. Sci. Part C: Polym. Symp.* **1967**, *16*, 2477.
(22) Mavrantzas, V. G.; Theodorou, D. N. *Macromolecules* **1998**, *31*, 6310.
(23) Dekmezian, D. E.; Axelson, D. E.; Dechter, J. J.; Borah, B.; Mandelkern, L. *J. Polym. Sci.* **1985**, *23*, 367.
(24) Zemke, K.; Schmidt-Rohr, K.; Spiess, H. W. *Acta Polym.* **1994**, *45*, 148.
(25) Smith, G. D.; Yoon, D. Y.; Zhu, W.; Ediger, M. D. *Macromolecules* **1994**, *27*, 5563.
(26) Weber, T. A.; Helfand, E. *J. Chem. Phys.* **1983**, *87*, 2881.
(27) Weiner, J. H. *Statistical Mechanics of Elasticity;* Wiley-Interscience: New York, 1983.

MA990888F